

Towards human SuperEEG

Lucy L. W. Owen¹, Andrew C. Heusser^{1,2}, and Jeremy R. Manning^{1*}

¹Department of Psychological and Brain Sciences, Dartmouth College,
Hanover, NH 03755, USA

²Akili Interactive,
Boston, MA 02110, USA

Abstract

Human *SuperEEG*¹ entails measuring ongoing neural activity with perfect precision and at arbitrarily high spatiotemporal resolution. Although true SuperEEG is impossible using existing methods, here we present a model-based method for *inferring* neural activity at millimeter-scale spatial resolutions and millisecond-scale temporal resolutions using standard human intracranial recordings. Our approach assumes that different people's brains exhibit similar spatial correlations, and that (all else being equal) neural activity at nearby locations will tend to be similar. One can then ask, for an arbitrary individual's brain: given recordings from a limited set of locations in that individual's brain, along with the observed spatial correlations learned from other people's recordings, how much can be inferred about ongoing activity at *other* locations in that individual's brain?

Keywords: Electrocorticography (ECoG), intracranial electroencephalography (iEEG), local field potential (LFP), epilepsy, maximum likelihood estimation, Gaussian process regression

Introduction

Modern human brain recording techniques are fraught with compromise [33]. Commonly used approaches include functional magnetic resonance imaging (fMRI), scalp electroencephalography (EEG), and magnetoencephalography (MEG). For each of these techniques, neuroscientists and electrophysiologists must choose to optimize spatial resolution at the cost of temporal resolution (e.g., as in fMRI) or temporal resolution at the cost of spatial resolution (e.g., as in EEG and MEG). A less widely used approach (due to requiring work with neurosurgical patients) is to record from electrodes implanted directly onto the cortical surface (electrocorticography; ECoG)

¹The term "SuperEEG" was coined by Robert J. Sawyer in his popular science fiction novel *The Terminal Experiment* [29]

25 or into deep brain structures (intracranial EEG; iEEG). However, these intracranial approaches
26 also require compromise: the high spatiotemporal resolutions of intracranial recordings comes
27 at the cost of substantially reduced brain coverage, since safety considerations limit the number
28 of electrodes one may implant in a given patient’s brain. Further, the locations of implanted
29 electrodes are determined by clinical, rather than research, needs.

30 An increasingly popular approach is to improve the effective spatial resolution of MEG or
31 scalp EEG data by using a geometric approach called *beamforming* to solve the biomagnetic or
32 bioelectrical inverse problem [28]. This approach entails using detailed brain conductance mod-
33 els (often informed by high spatial resolution anatomical MRI images) along with the known
34 sensor placements (localized precisely in 3D space) to reconstruct brain signals originating from
35 theoretical point sources deep in the brain (and far from the sensors). Traditional beamforming
36 approaches must overcome two obstacles. First, the inverse problem beamforming seeks to
37 solve has infinitely many solutions. Researchers have made traction towards constraining the
38 solution space by assuming that signal-generating sources are localized on a regularly spaced
39 grid spanning the brain and that individual sources are small relative to their distances to the
40 sensors [1, 11, 34]. The second, and in some ways much more serious, obstacle is that the
41 magnetic fields produced by external (noise) sources are substantially stronger than those pro-
42 duced by the neuronal changes being sought (i.e., at deep structures, as measured by sensors
43 at the scalp). This means that obtaining adequate signal quality often requires averaging the
44 measured responses over tens to hundreds of responses or trials (e.g., see review by [11]).

45 Another approach to obtaining high spatiotemporal resolution neural data has been to col-
46 lect fMRI and EEG data simultaneously. Simultaneous fMRI-EEG has the potential to balance
47 the high spatial resolution of fMRI with the high temporal resolution of scalp EEG, thereby,
48 in theory, providing the best of both worlds. In practice, however, the signal quality of both
49 recordings suffers substantially when the two techniques are applied simultaneously (e.g., see

50 review by [13]). In addition, the experimental designs that are ideally suited to each technique
51 individually are somewhat at odds. For example, fMRI experiments often lock stimulus presen-
52 tation events to the regularly spaced image acquisition time (TR), which maximizes the number
53 of post-stimulus samples. By contrast, EEG experiments typically employ jittered stimulus pre-
54 sentation times to maximize the experimentalist’s ability to distinguish electrical brain activity
55 from external noise sources such as from 60 Hz alternating current power sources.

56 The current “gold standard” for precisely localizing signals and sampling at high temporal
57 resolution is to take (ECoG or iEEG) recordings from implanted electrodes (but from a limited
58 set of locations in any given brain). This begs the following question: what can we infer
59 about the activity exhibited by the rest of a person’s brain, given what we learn from the
60 limited intracranial recordings we have from their brain and additional recordings taken from
61 *other* people’s brains? Here we develop an approach, which we call *SuperEEG*, based on
62 Gaussian process regression [27]. SuperEEG entails using data from multiple people to estimate
63 activity patterns at arbitrary locations in each person’s brain (i.e., independent of their electrode
64 placements). We test SuperEEG approach using two large datasets of intracranial recordings [7,
65 8, 12, 16–19, 21, 23, 30–32, 35, 40]. We show that the SuperEEG algorithm recovers signals well
66 from electrodes that were held out of the training dataset. We also examine the factors that
67 influence how accurately activity may be estimated (recovered), which may have important
68 implications for electrode design and placement in neurosurgical applications.

69 Approach

70 The SuperEEG approach to inferring high temporal resolution full-brain activity patterns is
71 outlined and summarized in Figure 1. We describe (in this section) and evaluate (in *Results*) our
72 approach using a two large previously collected dataset comprising multi-session intracranial
73 recordings. Dataset 1 comprises multi-session recordings taken from 6876 electrodes implanted

74 in the brains of 88 epilepsy patients [21, 23, 30–32]. Each recording session lasted from XXX–
75 XXX hours (Fig. S5A), and includes data recorded roughly from when the patients woke up
76 each morning, to before they went to sleep at the end of each day. In addition to typical
77 bed-ridden hospital patient activities (e.g., lying in bed, reading, watching television, using
78 personal electronic devices, listening to music, visiting with family and friends, etc.), the pa-
79 tients also performed a variety of experimental cognitive tasks throughout their day (primarily
80 list-learning memory tasks). For the purposes of the Dataset 1 analyses presented here, we
81 aggregated all data across each recording session, ignoring the particular activities or tasks
82 the patients were performing at any given moment. We used Dataset 1 to develop our main
83 SuperEEG approach, and to examine the extent to which SuperEEG might be able to generate
84 task-general predictions. Dataset 2 comprised multi-session recordings from XXX electrodes
85 implanted in the brains of XXX epilepsy patients [7, 8, 12, 16–19, 35, 40]. Each recording session
86 lasted from XXX–XXX hours (Fig. S5B). Whereas Dataset 1 included recordings taken during a
87 wide variety of behaviors, Dataset 2 included recordings taken as each patient performed each
88 of two memory tasks: a random word list free recall task and a categorized word list free recall
89 task. We used Dataset 2 to further examine the ability of SuperEEG to generalize its predictions
90 within versus across tasks. Figure S5 provides additional details on both datasets.

91 We first applied fourth order Butterworth notch filter to remove 60 Hz ($\pm .5$ Hz) line noise
92 from every recording (from every electrode). Next, we downsampled the recordings (regardless
93 of the original samplerate) to 250 Hz. (This downsampling step served to both normalize for
94 differences in sampling rates across patients and to ease the computational burden of our sub-
95 sequent analyses.) We then excluded any electrodes that showed putative epileptiform activity.
96 Specifically, we excluded from further analysis any electrode that exhibited an average kurtosis
97 of 10 or greater across all of that patient’s recording sessions. We also excluded any patients
98 with fewer than 2 electrodes that passed this criteria, as the SuperEEG algorithm requires

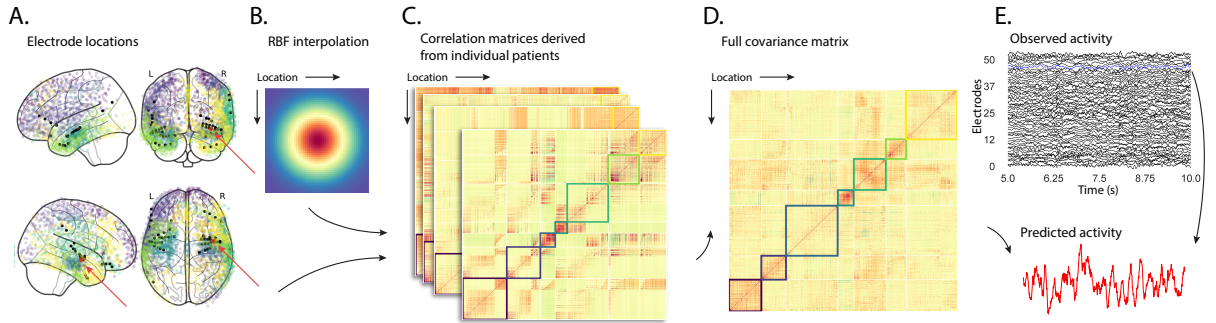


Figure 1: Methods overview. **A. Electrode locations.** Each dot reflects the location of a single electrode implanted in the brain of a Dataset 1 patient. A held-out recording location from one patient is indicated in red, and the patient’s remaining electrodes are indicated in black. The electrodes from the remaining patients are colored by k -means cluster (computed using the full-brain correlation model shown in Panel D). **B. Radial basis function kernel.** Each electrode contributed by the patient (black) weights on the full set of locations under consideration (all dots in Panel A, defined as \bar{R} in the text). The weights fall off with positional distance (in MNI space) according to an RBF. **C. Per-patient correlation matrices.** After computing the pairwise correlations between the recordings from each patient’s electrodes, we use RBF-weighted averages to estimate correlations between all locations in \bar{R} . We obtain an estimated full-brain correlation matrix using each patient’s data. **D. Merged correlation model.** We combine the per-patient correlation matrices (Panel C) to obtain a single full-brain correlation model that captures information contributed by every patient. Here we have sorted the rows and columns to reflect k -means clustering labels [using $k=7; 41$], whereby we grouped locations based on their correlations with the rest of the brain (i.e., rows of the matrix displayed in the panel). The boundaries denote the cluster groups. The rows and columns of Panel C have been sorted using the Panel D-derived cluster labels. **E. Reconstructing activity throughout the brain.** Given the observed recordings from the given patient (shown in black; held-out recording is shown in blue), along with a full-brain correlation model (Panel D), we use Equation 12 to reconstruct the most probable activity at the held-out location (red).

99 measuring correlations between 2 or more electrodes from each patient. For Dataset 1, this
100 yielded clean recordings from XXX electrodes implanted throughout the brains of XXX patients
101 (Fig. 1A); for Dataset 2, this yielded clean recordings from 2975 electrodes from 24 patients.
102 Each individual patient contributes electrodes from a limited set of brain locations, which we
103 localized in a common space [MNI152; 10]; an example Dataset 1 patient’s 54 electrodes that
104 passed the predefined kurtosis test are highlighted in black and red.

The recording from a given electrode is maximally informative about the activity of the neural tissue immediately surrounding its recording surface. However, brain regions that are distant from the recording surface of the electrode also contribute to the recording, albeit (*ceteris paribus*) to a much lesser extent. One mechanism underlying these contributions is volume conduction. The precise rate of falloff due to volume conduction (i.e., how much a small volume of brain tissue at location x contributes to the recording from an electrode at location η) depends on the size of the recording surface, the electrode’s impedance, and the conductance profile of the volume of brain between x and η . As an approximation of this intuition, we place a Gaussian radial basis function (RBF) at the location η of each electrode’s recording surface (Fig. 1B). We use the values of the RBF at any brain location x as a rough estimate of how much structures around x contributed to the recording from location η :

$$\text{rbf}(x|\eta, \lambda) = \exp \left\{ -\frac{\|x - \eta\|^2}{\lambda} \right\}, \quad (1)$$

105 where the width variable λ is a parameter of the algorithm (which may in principle be set
106 according to location-specific tissue conductance profiles) that governs the level of spatial
107 smoothing. In choosing λ for the analyses presented here, we sought to maximize spatial
108 resolution (which implies a small value of λ) while also maximizing the algorithm’s ability
109 to generalize to any location throughout the brain, including those without dense electrode
110 coverage (which implies a large value of λ). Using our prior work as a guide [22, 24], we set
111 $\lambda = 20$, although this could in theory be optimized, e.g., using cross validation or a formal

112 model [e.g., 24].

113 A second mechanism whereby a given region x can contribute to the recording at η is
114 through (direct or indirect) anatomical connections between structures near x and η . We use
115 temporal correlations in the data to estimate these anatomical connections [2]. Let \bar{R} be the
116 set of locations at which we wish to estimate local field potentials, and let $R_s \subseteq \bar{R}$ be set of
117 locations at which we observe local field potentials from patient s (excluding the electrodes that
118 did not pass the kurtosis test described above). In the analyses below we define $\bar{R} = \cup_{s=1}^S R_s$.
119 We can calculate the expected inter-electrode correlation matrix for patient s , where $C_{s,k}(i, j)$ is
120 the correlation between the time series of voltages for electrodes i and j from subject s during
121 session k , using:

$$\bar{C}_s = r\left(\frac{1}{n}\left(\sum_{k=1}^n z(C_{s,k})\right)\right), \text{ where} \quad (2)$$

$$z(r) = \frac{\log(1+r) - \log(1-r)}{2} \text{ is the Fisher } z\text{-transformation and} \quad (3)$$

$$z^{-1}(z) = r(z) = \frac{\exp(2z) - 1}{\exp(2z) + 1} \text{ is its inverse.} \quad (4)$$

122 Next, we use Equation 1 to construct a number of to-be-estimated locations by number of
123 patient electrode locations weight matrix, W_s . Specifically, W_s approximates how informative
124 the recordings at each location in R_s are in reconstructing activity at each location in \bar{R} , where
125 the contributions fall off with an RBF according to the distances between the corresponding
126 locations:

$$W_s(i, j) = \text{rbf}(i|j, \lambda). \quad (5)$$

127 Given this weight matrix, W_s , and the observed inter-electrode correlation matrix for patient
128 s , \bar{C}_s , we can estimate the correlation matrix for all locations in \bar{R} (\hat{C}_s ; Fig. 1C) using:

$$\hat{N}_s(x, y) = \sum_{i=1}^{|R_s|} \sum_{j=1}^{i-1} W(x, i) \cdot W(y, j) \cdot z(\bar{C}_s(i, j)) \quad (6)$$

$$\hat{D}_s(x, y) = \sum_{i=1}^{|R_s|} \sum_{j=1}^{i-1} W(x, i) \cdot W(y, j). \quad (7)$$

$$\hat{C}_s = r\left(\frac{\hat{N}_s}{\hat{D}_s}\right). \quad (8)$$

After estimating the numerator (\hat{N}_s) and denominator (\hat{D}_s) placeholders for each \hat{C}_s , we aggregate these estimates across the S patients to obtain a single expected full-brain correlation matrix (\hat{K} ; Fig. 1D):

$$\hat{K} = r\left(\frac{\sum_{s=1}^S \hat{N}_s}{\sum_{s=1}^S \hat{D}_s}\right). \quad (9)$$

129 Intuitively, the numerators capture the general structures of the patient-specific estimates of full-
 130 brain correlations, and the denominators account for which locations were near the implanted
 131 electrodes in each patient. To obtain \hat{K} , we compute a weighted average across the estimated
 132 patient-specific full-brain correlation matrices, where patients with observed electrodes near a
 133 particular set of locations in \hat{K} contribute more to the estimate.

134 Having used the multi-patient data to estimate a full-brain correlation matrix at the set
 135 of locations in \bar{R} that we wish to know about, we next use \hat{K} to estimate activity patterns
 136 everywhere in \bar{R} , given observations at only a subset of locations in \bar{R} (Fig. 1E).

137 Let α_s be the set of indices of patient s 's electrode locations in \bar{R} (i.e., the locations in R_s),
 138 and let β_s be the set of indices of all other locations in \bar{R} . In other words, β_s reflects the locations
 139 in \bar{R} where we did not observe a recording for patient s (these are the recording locations we
 140 will want to fill in using SuperEEG). We can sub-divide \hat{K} as follows:

$$\hat{K}_{\beta_s, \alpha_s} = \hat{K}(\beta_s, \alpha_s), \text{ and} \quad (10)$$

$$\hat{K}_{\alpha_s, \alpha_s} = \hat{K}(\alpha_s, \alpha_s). \quad (11)$$

141 Here $\hat{K}_{\beta_s, \alpha_s}$ represents the correlations between the “unknown” activity at the locations in β_s
 142 and the observed activity at the locations in α_s , and $\hat{K}_{\alpha_s, \alpha_s}$ represents the correlations between
 143 the observed recordings (at the locations in α_s).

144 Let Y_{s,k,α_s} be the number-of-timepoints (T) by $|\alpha_s|$ matrix of (observed) voltages from the
 145 electrodes in α_s during session k from patient s . Then we can estimate the voltage from patient
 146 s ’s k^{th} session at the locations in β_s using [27]:

$$\hat{Y}_{s,k,\beta_s} = ((\hat{K}_{\beta_s, \alpha_s} \cdot \hat{K}_{\alpha_s, \alpha_s}^{-1}) \cdot Y_{s,k,\alpha_s}^T)^T. \quad (12)$$

147 This equation is the foundation of the SuperEEG algorithm. Whereas we observe recordings
 148 only at the locations indexed by α_s , Equation 12 allows us to estimate the recordings at all loca-
 149 tions indexed by β_s , which we can define *a priori* to include any locations we wish, throughout
 150 the brain. This yields estimates of the time-varying voltages at *every* location in \bar{R} , provided that
 151 we define \bar{R} in advance to include the union of all of the locations in R_s and all of the locations
 152 at which we wish to estimate recordings (i.e., a timeseries of voltages).

153 We designed our approach to be agnostic to electrode impedances, as electrodes that do not
 154 exist do not have impedances. Therefore our algorithm recovers voltages in standard deviation
 155 (z -scored) units rather than attempting to recover absolute voltages. (This property reflects
 156 the fact that $\hat{K}_{\beta_s, \alpha_s}$ and $\hat{K}_{\alpha_s, \alpha_s}$ are correlation matrices rather than covariance matrices.) Also,
 157 note that Equation 12 requires computing a T by T matrix, which can become computationally
 158 intractable when T is very large (e.g., for the patient highlighted in Fig. 2, $T = 20458799$).

159 However, because Equation 12 is time invariant, we may compute Y_{s,k,β_s} in a piecewise manner
160 by filling in Y_{s,k,β_s} one row at a time (using the corresponding samples from Y_{s,k,α_s}).

161 The SuperEEG algorithm described above and in Figure 1 allows us to estimate, up to a
162 constant scaling factor, local field potentials (LFPs) for each patient at all arbitrarily chosen
163 locations in the set \bar{R} , even if we did not record that patient's brain at all of those locations. We next
164 turn to an evaluation of the accuracy of those estimates.

165 Results

166 We used a cross-validation approach to test the accuracy with which the SuperEEG algorithm
167 reconstructs activity throughout the brain. For each patient in turn, we estimated full-brain
168 correlation matrices (Eqn. 9) using data from all of the *other* patients. This step ensured that the
169 data we were reconstructing could not also be used to estimate the between-location correlations
170 that drove the reconstructions via Equation 12 (otherwise the analysis would be circular). For
171 that held-out patient, for each of their electrodes in turn, we used Equation 12 to reconstruct
172 activity at the held-out electrode location, using the correlation matrix learned from all other
173 patients' data as \hat{K} , and using activity recorded from the other electrodes from the held-out
174 patient as Y_{s,k,α_s} . We then asked: how closely did each of the SuperEEG-estimated recordings
175 at those electrodes match the observed recordings from those electrodes (i.e., how closely did
176 the estimated \hat{Y}_{s,k,β_s} match the observed Y_{s,k,β_s} ?).

177 To illustrate our approach, we first examine an individual held-out raw LFP trace and
178 its associated SuperEEG-derived reconstruction. Figure 2A displays the observed LFP from
179 the red electrode in Figure 1A (red), and its associated reconstruction (blue), during a 5 s time
180 window during one of the example patient's six recording sessions. The two traces match closely
181 ($r = XXX, p = XXX$). Figure 2B displays a two-dimensional histogram of the actual versus
182 reconstructed voltages for the entire 14.2 total hours of recordings from the example electrode

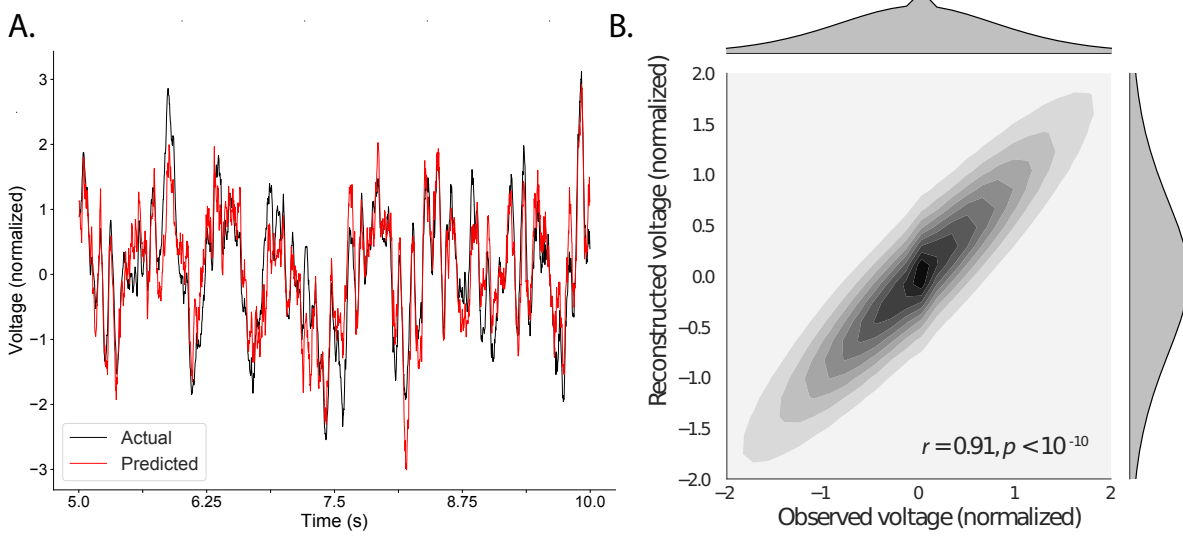


Figure 2: Observed and reconstructed LFP from a single electrode. **A. Example LFP.** A 5 s recording from the red electrode in Figure 1A is displayed in red, and the reconstructed LFP during the same time window is shown in blue. **B. Observed versus reconstructed LFP over 14.2 hours.** The two-dimensional histogram reflects the relation between distributions of observed versus reconstructed voltages from one patient, across the 14.2 hours of recorded data collected over 6 recording sessions. The correlation reported in the panel is between the observed and reconstructed voltages. Both panels: all voltages are represented in standard deviation units (computed within session).

(correlation: $r = XXX, p = XXX$). This example confirms that the SuperEEG algorithm recovers the recordings from this single electrode well. Next, we used this general approach to quantify the algorithm's performance across the full dataset.

For each held-out electrode, from each held-out patient in turn, we computed the average correlation (across recording sessions) between the SuperEEG-reconstructed voltage traces and the observed voltage traces from that electrode. For this analysis we set \bar{R} to be the union of all electrode locations across all patients. This yielded a single correlation coefficient for each electrode location in \bar{R} , reflecting how well the SuperEEG algorithm was able to recover the recording at that location by incorporating data across patients (black histogram in Fig. 3A, map in Fig. 3C). The observed distribution of correlations was centered well above zero (mean: XXX;

193 t -test comparing mean of distribution of z -transformed per-electrode correlation coefficients
194 to 0: $t(XXX) = XXX, p = XXX$, indicating that the SuperEEG algorithm recovers held-out
195 activity patterns substantially better than random guessing.

196 As a stricter benchmark, we compared the quality of these across-participant reconstructions
197 (i.e., computed using a correlation model learned from other patients' data) to reconstructions
198 generated using a correlation model trained using the in-patient's data. In other words, for
199 this within-patient benchmark analysis we estimated \hat{C}_s (Eqn. 8) for each patient in turn, using
200 recordings from all of that patient's electrodes except at the location we were reconstructing.
201 These within-patient reconstructions serve as an estimate of how well data from all of the
202 other electrodes from that single patient may be used to estimate held-out data from the
203 same patient. This allows us to ask how much information about the activity at a given
204 electrode might be inferred through (a) volume conductance or other sources of "leakage"
205 from activity patterns measured from the patient's other electrodes and (b) across-electrode
206 correlations learned from that single patient. As shown in Figure 3A (gray histogram), the
207 distribution of within-patient correlations was centered well above zero (mean: XXX; t -test
208 comparing mean of distribution of z -transformed per-electrode correlation coefficients to 0:
209 $t(XXX) = XXX, p = XXX$). However, the across-patient correlations were substantially higher
210 (t -test comparing average z -transformed within versus across patient electrode correlations:
211 $t(XXX) = XXX, p = XXX$). This is an especially conservative test, given that the across-patient
212 SuperEEG reconstructions exclude (from the correlation matrix estimates) all data from the
213 patient whose data is being reconstructed. We repeated each of these analyses on a second
214 independent dataset and found similar results (Fig. 3B, D; within versus across reconstruction
215 accuracy: $t(23) = 6.93, p < 10^{-5}$). We also replicated this result separately for each of the two
216 experiments from Dataset 2 (Fig. S2). This overall finding, that reconstructions of held-out
217 data using correlation models learned from *other* patient's data yield higher reconstruction

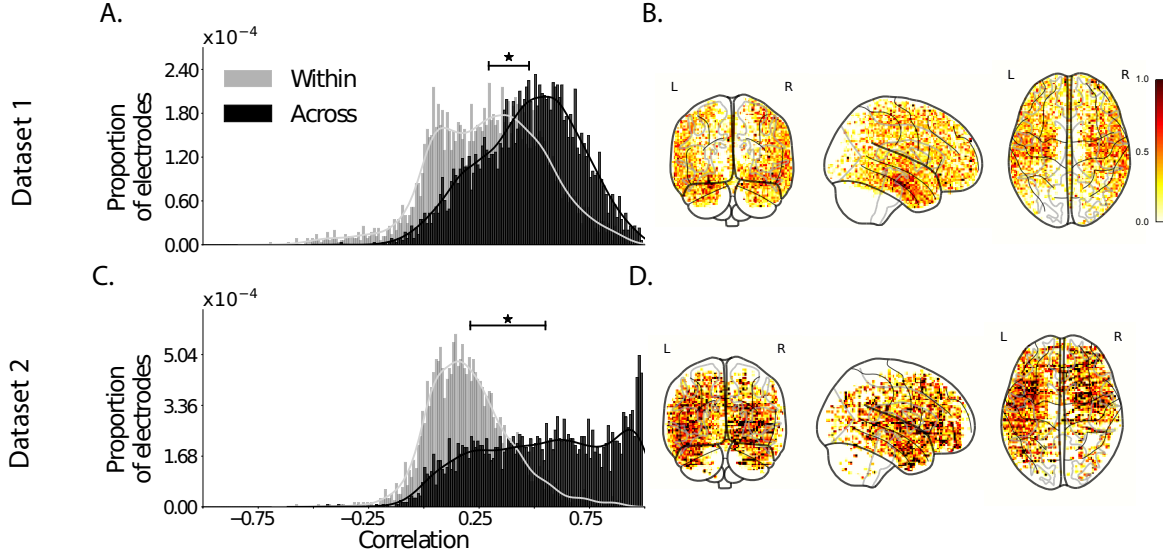


Figure 3: Reconstruction quality across all electrodes in two ECoG datasets. A. Distributions of correlations between observed versus reconstructed activity by electrode, for Dataset 1. The across-patient distribution (black) reflects reconstruction accuracy (correlation) using a correlation model learned from all but one patient's data, and then applied to that held-out patient's data. The within-patient distribution (gray) reflects performance using a correlation model learned from the same patient who contributed the to-be-reconstructed electrode. **B. Distributions of correlations for Dataset 2.** This panel is in the same format as Panel A, but reflects results obtained from Dataset 2. The histograms aggregate data across both Dataset 2 experiments; for results broken down by experiment see Figure S4. **C.-D. Reconstruction performance by location.** Each dot reflects the location of a single implanted electrode from Dataset 1 (Panel C) or Dataset 2 (Panel D). The dot colors denote the average across-session correlation, using the across-patient correlation model, between the observed and reconstructed activity at the given electrode location.

accuracy than correlation models learned from the patient whose data is being reconstructed, has two important implications. First, it implies that distant electrodes provide additional predictive power to the data reconstructions beyond the information contained solely in nearby electrodes. (This follows from the fact that each patient's electrodes are implanted in a unique set of locations, so for any given electrode the closest electrodes in the full dataset are likely to come from the same patient.) Second, it implies that the spatial correlations learned using the SuperEEG algorithm are, to some extent, similar across people.

225 The recordings we analyzed from Dataset 1 comprised data collected as the patients per-
226 formed a variety of (largely idiosyncratic) tasks throughout each day’s recording session. That
227 we observed reliable reconstruction accuracy across patients suggests that the spatial correla-
228 tions derived from the SuperEEG algorithm are, to some extent, similar across tasks. We tested
229 this finding more explicitly using Dataset 2. In Dataset 2, the recordings were limited to times
230 when each patient was participating in each of two experiments (Experiment 1, a random-word
231 list free recall task, and Experiment 2, a categorized list free recall task). We wondered whether
232 a correlation model learned from data from one experiment might yield good predictions of
233 data from the other experiment. Further, we wondered about the extent to which it might be
234 beneficial or harmful to combine data across tasks.

235 To test the task-specificity of the SuperEEG-derived correlation models, we repeated the
236 above within- and across-patient cross validation procedures separately for Experiment 1 and
237 Experiment 2 data from Dataset 2. We then compared the reconstruction accuracies for held-out
238 electrodes, for models trained within versus across the two experiments, or combining across
239 both experiments (Fig. S3). In every case we found that across-patient models trained using
240 data from all other patients out-performed within-patient models trained on data only from
241 the subject contributing the given electrode ($ts(XXX) > XXX, ps < XXX$). All reconstruction
242 accuracies also reliably exceeded chance performance ($ts(XXX) > XXX, ps < XXX$). Average
243 reconstruction accuracy was highest for the across-patient models limited to data from the same
244 experiment (mean accuracy: 0.55); next-highest for the across-patient models that combined
245 data across both experiments (mean accuracy: 0.50); and lowest for models trained across task
246 (mean accuracy: 0.37). This result also held for each of the Dataset 2 experiments individually
247 (Fig. S4). Taken together, these results indicate that there are reliable commonalities in the spatial
248 correlations of full-brain activity across tasks, but that there are also reliable differences in these
249 spatial correlations across tasks. Whereas reconstruction accuracy benefits from incorporating

250 data from other patients, reconstruction accuracy is highest when constrained to within-task
251 data, or data that includes a variety of tasks (e.g., Dataset 1, or combining across the two Dataset
252 2 experiments).

253 Although both datasets we examined provide good full-brain coverage (when considering
254 data from every patient; e.g. Fig. 3C, D), electrodes are not placed uniformly throughout the
255 brain. For example, electrodes are more likely to be implanted in regions like the medial
256 temporal lobe (MTL), and are rarely implanted in occipital cortex (Fig. 4A, B). Separately for
257 each dataset, for each voxel in the 4 mm³ voxel MNI152 brain, we computed the proportion
258 of electrodes in the dataset that were contained within a 20 MNI unit radius sphere centered
259 on that voxel. We defined the *density* at that location as this proportion. Across Datasets 1
260 and 2, the electrode placement densities were similar (correlation by voxel: $r = XXX, p =$
261 XXX). We wondered whether regions with good coverrage might be associated with better
262 reconstruction accuracy (e.g. Fig. 3C, D indicate that many electrodes in the MTL have relatively
263 high reconstruction accuracy, and occipital electrodes tend to have relatively low reconstruction
264 accuracy). To test whether this held more generally across the entire brain, for each dataset
265 we computed the electrode placement density for each electrode from each patient (using
266 the proportion of *other* patients' electrodes within 20 MNI units of the given electrode). We
267 then correlated these density values with the across-patient reconstruction accuracies for each
268 electrode. Contrary to our expectation, rather than positive correlations, we found weak (but
269 reliable) negative correlations between reconstruction accuracy and density for both datasets
270 (Dataset 1: $r = XXX, p = XXX$; Dataset 2: $r = -0.16, p < 10^{-10}$). This indicates that the
271 reconstruction accuracies we observed are not driven solely by sampling density, but rather
272 may also reflect higher order properties of neural dynamics such as functional correlations
273 between distant voxels [3].

274 In neurosurgical applications where one wishes to infer full-brain activity patterns, can our

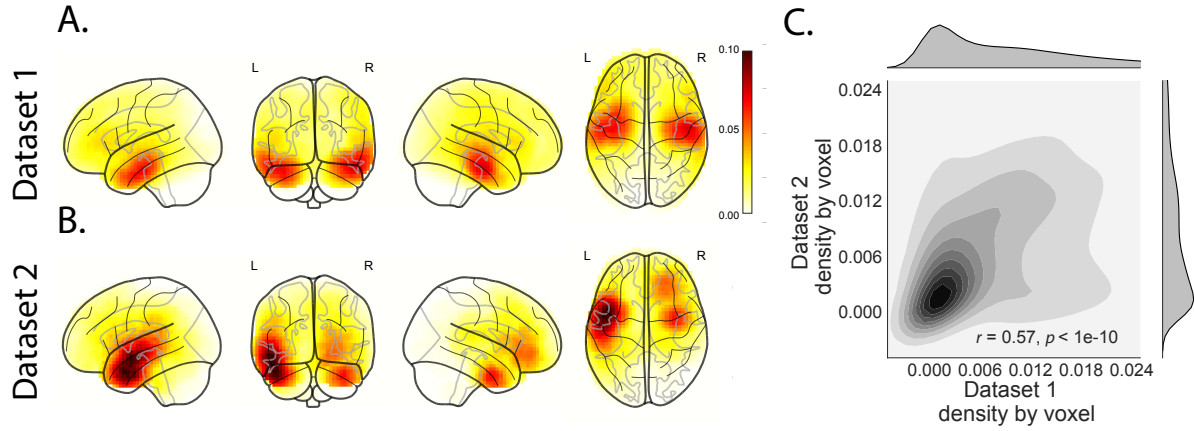


Figure 4: Electrode sampling density by location. **A. Electrode sampling density by voxel in Dataset 1.** Each voxel is colored by the proportion of total electrodes in the dataset that are located within a 20 MNI unit radius sphere centered on the given voxel. **B. Electrode sampling density by voxel in Dataset 2.** This panel displays the sampling density map for Dataset 2, in the same format as Panel A. **C. Correspondence in sampling density by voxel across Datasets 1 and 2.** The two-dimensional histogram displays the by-voxel densities in the two Datasets, and the one-dimensional histograms display the proportions of voxels in each dataset with the given density value. The correlation reported in the panel is across voxels in the 4 mm^3 MNI brain.

275 framework yield insights into where the electrodes should be placed? A basic assumption of our
 276 approach (and of most prior ECoG work) is that electrode recordings are most informative about
 277 the neural activity near the recording surface of the electrode. But if we consider that activity
 278 patterns throughout the brain are meaningfully correlated, are there particular implantation
 279 locations that, if present in a patient's brain, yield especially high reconstruction accuracies
 280 throughout the rest of the brain? For example, one might hypothesize that brain structures
 281 that are heavily interconnected with many other structures could be more informative about
 282 full-brain activity patterns than comparatively isolated structures.

283 To gain insights into whether particular electrode locations might be especially informative,
 284 we first computed the average reconstruction accuracy across all of each patient's electrodes
 285 (using the across-patients cross validation test; black histograms in Fig. 3A and B). We labeled
 286 each patient's electrodes in each dataset with the average reconstruction accuracy for that

287 patient. In other words, we assigned every electrode from each given patient the same value,
288 reflecting how well the activity patterns at those electrodes were reconstructed on average.
289 Next, for each voxel in the 4 mm³ MNI brain, we computed the average value across any
290 electrode (from any patient) that came within 20 MNI units of that voxel’s center. Effectively,
291 we computed an *information score* for each voxel, reflecting the average reconstruction accuracy
292 across any patients with electrodes near each voxel—where the averages were weighted to reflect
293 patients who had more electrodes implanted near that location. This yielded a single map for
294 each dataset, highlighting regions that are potentially promising implantation targets in terms
295 of providing full-brain activity information via SuperEEG (Fig. 5A, B). Despite task and patient
296 differences across the two datasets, we nonetheless found that the maps of the most promising
297 implantation targets derived from both datasets were similar (voxelwise correlation between
298 information scores across the two datasets: $r = XXX, p = XXX$). While the correspondence
299 between the two maps was not perfect, our finding that there were some commonalities between
300 the two maps lends support to the notion that different brain areas are differently informative
301 about full-brain activity patterns. Further, regions like XXX, XXX, and XXX that exhibited
302 strong information scores in both datasets may be especially promising implantation targets.

303 Discussion

304 Are our brain’s networks static or dynamic? And to what extent are the network properties
305 of our brains stable across people and tasks? One body of work suggests that our brain’s
306 *functional* networks are dynamic [e.g., 24], person-specific [e.g., 9], and task-specific [e.g.,
307 39]. In contrast, although the gross anatomical structure of our brains changes meaningfully
308 over the course of years as our brains develop, on the timescales of typical neuroimaging ex-
309 periments (i.e., hours to days) our anatomical networks are largely stable [e.g., 4]. Further,
310 many aspects of brain anatomy, including white matter structure, is largely preserved across

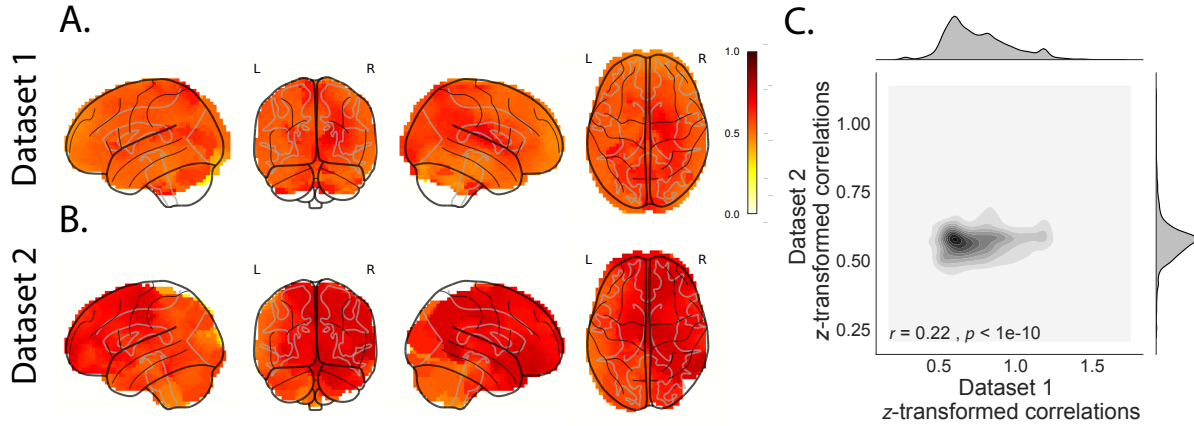


Figure 5: Most informative electrode locations. **A. Dataset 1 information score by voxel.** The voxel colors reflect the weighted average reconstruction accuracy across all electrodes from any patients with at least one electrode within 20 MNI units of the given voxel. **B. Dataset 2 information score by voxel.** This panel is in the same format as Panel A. **C. Correspondence in information scores by voxel across Datasets 1 and 2.** Same format as Figure 4C.

311 people [e.g., 15, 26, 37] There are several possible means of reconciling this apparent inconsis-
 312 tency between dynamic person- and task-specific functional networks versus stable anatomical
 313 networks. For example, relatively small magnitude anatomical differences across people may
 314 be reflected in reliable functional connectivity differences. Along these lines, one recent study
 315 found that diffusion tensor imaging (DTI) structural data is similar across people, but may be
 316 used to predict person-specific resting state functional connectivity data [2]. Similarly, other
 317 work indicates that task-specific functional connectivity may be predicted by resting state func-
 318 tional connectivity data [5, 38]. Another (potentially complementary) possibility is that our
 319 functional networks are constrained by anatomy, but nevertheless exhibit (potentially rapid)
 320 task-dependent changes [e.g., 36].

321 Here we have taken a model-based approach to studying whether high spatiotemporal
 322 resolution activity patterns throughout the human brain may be explained by a static connec-
 323 tome model that is shared across people and tasks. Specifically, we trained a model to take
 324 in recordings from a subset of brain locations, and then predicted activity patterns during the

325 same interval, but at *other* locations that were held out from the model. Our model, based on
326 Gaussian process regression, was built on three general hypotheses about the nature of the
327 correlational structure of neural activity (each of which we tested). First, we hypothesized that
328 functional correlations are stable over time and across tasks. We found that, although aspects
329 of the patients' functional correlations that were stable across tasks, we achieved better recon-
330 struction accuracy when we trained the model on within-task data [we acknowledge that our
331 general approach could potentially be extended to better model across-task changes, following
332 5, 38, and others]. Second, we hypothesized that some of the correlational structure of peo-
333 ple's brain activity is similar across individuals. Consistent with this hypothesis, our model
334 explained the data best when we trained the correlation model using data from *other* patients–
335 even when compared to a correlation model trained on the same patient's data. Third, we
336 resolved ambiguities in the data by hypothesizing that neural activity from nearby sources will
337 tend to be similar, all else being equal. This hypothesis was supported through our finding that
338 all of the models we trained that incorporated this spatial smoothness assumption predicted
339 held-out data well above chance.

340 One potential limitation of our approach is that it does not provide a natural means of
341 estimating the precise timing of single-neuron action potentials. Prior work has shown that
342 gamma band and broadband activity in the LFP may be used to estimate the firing rates of
343 neurons that underly the population contributing to the LFP [6, 14, 20, 25]. Because SuperEEG
344 reconstructs LFPs throughout the brain, one could in principle use gamma or broadband power
345 in the reconstructed signals to estimate the corresponding firing rates (though not the timings
346 of individual action potentials).

347 Beyond providing a means of estimating ongoing activity throughout the brain using al-
348 ready implanted electrodes, our work also has implications for where to place the electrodes in
349 the first place. Electrodes are typically implanted to maximize coverage of suspected epilep-

350 togenic tissue. However, our findings suggest that this approach could be further optimized.
351 Specifically, one could leverage not only the non-invasive recordings taken during an initial
352 monitoring period (as is currently done routinely), but also recordings collected from other
353 patients. We could then ask: given what we learn from other patients' data (and potentially
354 from the scalp EEG recordings of this new patient), where should we place a fixed number of
355 electrodes to maximize our ability to map seizure foci? As shown in Figure 5, recordings from
356 different locations are differently informative in terms of reconstructing the spatiotemporal
357 activity patterns throughout the brain. This property might be leveraged in decisions about
358 where to surgically implant electrodes in future patients.

359 **Concluding remarks**

360 Over the past several decades, neuroscientists have begun to leverage the strikingly profound
361 mathematical structure underlying the brain's complexity to infer how our brains carry out
362 computations to support our thoughts, actions, and physiological processes. Whereas tradi-
363 tional beamforming techniques rely on geometric source-localization of signals measured at the
364 scalp, here we propose an alternative approach that leverages the rich correlational structure
365 of two large datasets of human intracranial recordings. In doing so, we are one step closer to
366 observing, and perhaps someday understanding, the full spatiotemporal structure of human
367 neural activity.

368 **Code availability**

369 We have published an open-source toolbox implementing the SuperEEG algorithm. It may be
370 downloaded [here](#).

³⁷¹ **Data availability**

³⁷² The dataset analyzed in this study was generously shared by Michael Kahana. A portion of
³⁷³ Dataset 1 may be downloaded [here](#). Dataset 2 may be downloaded [here](#).

³⁷⁴ **Acknowledgements**

³⁷⁵ We are grateful for useful discussions with Luke J. Chang, Uri Hasson, Josh Jacobs, Michael
³⁷⁶ Kahana, and Matthijs van der Meer. We are also grateful to Michael Kahana for generously
³⁷⁷ sharing the ECoG data we analyzed in our paper, which was collected under NIMH grant
³⁷⁸ MH55687 and DARPA RAM Cooperative Agreement N66001-14-2-4-032, both to MJK. Our
³⁷⁹ work was also supported in part by NSF EPSCoR Award Number 1632738 and by a sub-
³⁸⁰ award of DARPA RAM Cooperative Agreement N66001-14-2-4-032 to JRM. The content is solely
³⁸¹ the responsibility of the authors and does not necessarily represent the official views of our
³⁸² supporting organizations.

³⁸³ **Author Contributions**

³⁸⁴ J.R.M conceived and initiated the project. L.L.W.O. and A.C.H. performed the analyses. J.R.M.
³⁸⁵ and L.L.W.O. wrote the manuscript.

³⁸⁶ **Author Information**

³⁸⁷ Reprints and permissions information is available at www.nature.com/reprints. The authors
³⁸⁸ declare no competing financial interests. Readers are welcome to comment on the online
³⁸⁹ version of the paper. Publisher's note: Springer Nature remains neutral with regard to jurisdic-
³⁹⁰ tional claims in published maps and institutional affiliations. Correspondence and requests for
³⁹¹ materials should be addressed to J.R.M. (jeremy.r.manning@dartmouth.edu).

392 **References**

- 393 [1] Baillet, S., Mosher, J. C., and Leahy, R. M. (2001). Electromagnetic brain mapping. *IEEE*
394 *Signal Processing Magazine*, 18:14–30.
- 395 [2] Becker, C. O., Pequito, S., Pappas, G. J., Miller, M. B., adn D S Bassett, S. T. G., and Preciado,
396 V. M. (2018). Spectral mapping of brain functional connectivity from diffusion imaging.
397 *Scientific Reports*, 8(1411):<https://www.doi.org/10.1038/s41598-017-18769-x>.
- 398 [3] Betzel, R. F., Medaglia, J. D., Kahn, A. E., Soffer, J., Schonhaut, D. R., and Bassett, D. S.
399 (2017). Inter-regional ecog correlations predicted by communication dynamics, geometry,
400 and correlated gene expression. *arXiv*, page 1706.06088.
- 401 [4] Casey, B. J., Giedd, J. N., and Thomas, K. M. (2000). Structural and functional brain devel-
402 opment and its relation to cognitive development. *Biological Psychology*, 54(1–3):241–257.
- 403 [5] Cole, M. W., Ito, T., Bassett, D. S., and Schultz, D. H. (2016). Activity flow over resting-state
404 networks shapes cognitive task activations. *Nature Neuroscience*, 19(12):1718–1726.
- 405 [6] Crone, N. E., Korzeniewska, A., and Franaszczuk, P. (2011). Cortical gamma responses:
406 searching high and low. *International Journal of Psychophysiology*, 79(1):9–15.
- 407 [7] Ezzyat, Y., Kragel, J. E., Burke, J. F., Levy, D. F., Lyalenko, A., Wanda, P., O’Sullivan, L.,
408 Hurley, K. B., Busygin, S., Pedisich, I., Sperling, M. R., Worrell, G. A., Kucewicz, M. T., Davis,
409 K. A., Lucas, T. H., Inman, C. S., Lega, B. C., Jobst, B. C., Sheth, S. A., Zaghloul, K., Jutras,
410 M. J., Stein, J. M., Das, S. R., Gorniak, R., Rizzuto, D. S., and Kahana, M. J. (2017). Direct
411 brain stimulation modulates encoding states and memory performance in humans. *Current
412 Biology*, 27:1–8.
- 413 [8] Ezzyat, Y., Wanda, P. A., Levy, D. F., Kadel, A., Aka, A., Pedisich, I., Sperling, M. R.,

- 414 Sharan, A. D., Lega, B. C., Burks, A., Gross, R. E., Inman, C. S., Jobst, B. C., Goren-
415 stein, M. A., Davis, K. A., Worrell, G. A., Kucewicz, M. T., Stein, J. M., Gorniak, R.,
416 Das, S. R., Rizzuto, D. S., and Kahana, M. J. (2018). Closed-loop stimulation of tem-
417 poral cortex rescues functional networks and improves memory. *Nature Communications*,
418 9(365):<https://doi.org/10.1038/s41467-017-02753-0>.
- 419 [9] Finn, E. S., Shen, X., Scheinost, D., Rosenberg, M. D., Huang, J., Chun, M. M., Papademetris,
420 X., and Constable, R. T. (2015). Functional connectome fingerprinting: identifying individuals
421 using patterns of brain connectivity. *Nature Neuroscience*, 18:1664 – 1671.
- 422 [10] Grabner, G., Janke, A. L., Budge, M. M., Smith, D., Pruessner, J., and Collins, D. L. (2006).
423 Symmetric atlasing and model based segmentation: an application to the hippocampus in
424 older adults. *Medical Image Computing and Computer-Assistend Intervention*, 9:58–66.
- 425 [11] Hillebrand, A., Singh, K. D., Holliday, I. E., Furlong, P. L., and Barnes, G. R. (2005). A new
426 approach to neuroimaging with magnetoencephalography. *Human Brain Mapping*, 25:199–
427 211.
- 428 [12] Horak, P. C., Meisenhelter, S., Song, Y., Testorf, M. E., Kahana, M. J., Viles, W. D., Bujarski,
429 K. A., Connolly, A. C., Robbins, A. A., Sperling, M. R., Sharan, A. D., Worrell, G. A., Miller,
430 L. R., Gross, R. E., Davis, K. A., Roberts, D. W., Lega, B., Sheth, S. A., Zaghloul, K. A., Stein,
431 J. M., Das, S. R., Rizzuto, D. S., and Jobst, B. C. (2017). Interictal epileptiform discharges
432 impair word recall in multiple brain areas. *Epilepsia*, 58(3):373–380.
- 433 [13] Huster, R. J., Debener, S., Eichele, T., and Herrmann, C. S. (2012). Methods for simultaneous
434 EEG-fMRI: an introductory review. *The Journal of Neuroscience*, 32(18):6053–6060.
- 435 [14] Jacobs, J., Kahana, M. J., Ekstrom, A. D., Mollison, M. V., and Fried, I. (2010). A sense of

- 436 direction in human entorhinal cortex. *Proceedings of the National Academy of Sciences, USA*,
437 107(14):6487–6482.
- 438 [15] Jahanshad, N., Kochunov, P. V., Sprooten, E., Mandl, R. C., Nichols, T. E., Almasy, L.,
439 Blangero, J., Brouwer, R. M., Curran, J. E., de Zubicaray, G. I., Duggirala, R., Fox, P. T., Hong,
440 L. E., Landman, B. A., Martin, N. G., McMahon, K. L., Medland, S. E., Mitchell, B. D., Olvera,
441 R. L., Peterson, C. P., Starr, J. M., Sussmann, J. E., Toga, A. W., Wardlaw, J. M., Wright, M. J.,
442 Pol, H. E. H., Pastin, M. E., McIntosh, A. M., Deary, I. J., Thompson, P. M., and Glahn, D. C.
443 (2013). Multi-site genetic analysis of diffusion images and voxelwise heritability analysis: A
444 pilot project of the enigma-dti working group. *NeuroImage*, 81(1):455–469.
- 445 [16] Kragel, J. E., Ezzyat, Y., Sperling, M. R., Gorniak, R., Worrell, G. A., Berry, B. M., Inman,
446 C., Lin, J.-J., Davis, K. A., Das, S. R., Stein, J. M., Jobst, B. C., Zaghloul, K. A., Sheth, S. A.,
447 Rizzuto, D. S., and Kahana, M. J. (2017). Similar patterns of neural activity predict memory
448 formation during encoding and retrieval. *NeuroImage*, 155:70–71.
- 449 [17] Kucewicz, M. T., Berry, B. M., Kremen, V., Brinkmann, B. H., Sperling, M. R., Jobst, B. C.,
450 Gross, R. E., Lega, B., Sheth, S. A., Stein, J. M., Das, S. R., Gorniak, R., Stead, S. M., Rizzuto,
451 D. S., Kahana, M. J., and Worrell, G. A. (2017). Dissecting gamma frequency actiivty during
452 human memory processing. *Brain*, 140:1337–1350.
- 453 [18] Kucewicz, M. T., Berry, B. M., Miller, L. R., Khadjevand, F., Ezzyat, Y., Stein, J. M., Kremen,
454 V., Brinkmann, B. H., Wanda, P., Sperling, M. R., Gorniak, R., Davis, K. A., Jobst, B. C., Gross,
455 R. E., Lega, B., Gompel, J. V., Stead, S. M., Rizzuto, D. S., Kahana, M. J., and Worrell, G. A.
456 (2018). Evidence for verbal memory enhancement with electrical brain stimulation in the
457 lateral temporal cortex. *Brain*, 141(4):971–978.
- 458 [19] Lin, J.-J., Rugg, M. D., Das, S., Stein, J., Rizzuto, D. S., Kahana, M. J., and Lega, B. C.

- 459 (2017). Theta band power increases in the posterior hippocampus predict successful episodic
460 memory encoding in humans. *Hippocampus*, 27:1040–1053.
- 461 [20] Manning, J. R., Jacobs, J., Fried, I., and Kahana, M. J. (2009). Broadband shifts in LFP power
462 spectra are correlated with single-neuron spiking in humans. *The Journal of Neuroscience*,
463 29(43):13613–13620.
- 464 [21] Manning, J. R., Polyn, S. M., Baltuch, G., Litt, B., and Kahana, M. J. (2011). Oscillatory
465 patterns in temporal lobe reveal context reinstatement during memory search. *Proceedings of*
466 *the National Academy of Sciences, USA*, 108(31):12893–12897.
- 467 [22] Manning, J. R., Ranganath, R., Norman, K. A., and Blei, D. M. (2014). Topographic
468 factor analysis: a Bayesian model for inferring brain networks from neural data. *PLoS One*,
469 9(5):e94914.
- 470 [23] Manning, J. R., Sperling, M. R., Sharan, A., Rosenberg, E. A., and Kahana, M. J. (2012).
471 Spontaneously reactivated patterns in frontal and temporal lobe predict semantic clustering
472 during memory search. *The Journal of Neuroscience*, 32(26):8871–8878.
- 473 [24] Manning, J. R., Zhu, X., Willke, T. L., Ranganath, R., Stachenfeld, K., Hasson, U., Blei,
474 D. M., and Norman, K. A. (2018). A probabilistic approach to discovering dynamic full-brain
475 functional connectivity patterns. *NeuroImage*.
- 476 [25] Miller, K. J., Shenoy, P., den Nijs, M., Sorensen, L. B., Rao, R. P. N., and Ojemann, J. G. (2008).
477 Beyond the gamma band: the role of high-frequency features in movement classification.
478 *IEEE Transactions on Biomedical Engineering*, 55(5):1634 – 1637.
- 479 [26] Mori, S., Oishi, K., Jiang, H., Jiang, L., Li, X., Akhter, K., Hua, K., Faria, A. V., Mahmood,
480 A., Woods, R., Toga, A. W., Pike, G. B., Neto, P. R., Evans, A., Zhang, J., Huang, H., Miller,

- 481 M. I., van Zijl, P., and Mazziotta, J. (2008). Stereotaxic white matter atlas based on diffusion
482 tensor imaging in an icbm template. *NeuroImage*, 40(2):570–582.
- 483 [27] Rasmussen, C. E. (2006). *Gaussian processes for machine learning*. MIT Press.
- 484 [28] Sarvas, J. (1987). Basic mathematical and electromagnetic concepts of the biomagnetic
485 inverse problem. *Phys. Med. Biol.*, 32(1):11–22.
- 486 [29] Sawyer, R. J. (1995). *The Terminal Experiment*. HarperPrism.
- 487 [30] Sederberg, P. B., Kahana, M. J., Howard, M. W., Donner, E. J., and Madsen, J. R. (2003). Theta
488 and gamma oscillations during encoding predict subsequent recall. *Journal of Neuroscience*,
489 23(34):10809–10814.
- 490 [31] Sederberg, P. B., Schulze-Bonhage, A., Madsen, J. R., Bromfield, E. B., Litt, B., Brandt,
491 A., and Kahana, M. J. (2007a). Gamma oscillations distinguish true from false memories.
492 *Psychological Science*, 18(11):927–932.
- 493 [32] Sederberg, P. B., Schulze-Bonhage, A., Madsen, J. R., Bromfield, E. B., McCarthy, D. C.,
494 Brandt, A., Tully, M. S., and Kahana, M. J. (2007b). Hippocampal and neocortical gamma
495 oscillations predict memory formation in humans. *Cerebral Cortex*, 17(5):1190–1196.
- 496 [33] Sejnowski, T. J., Churchland, P. S., and Movshon, J. A. (2014). Putting big data to good use
497 in neuroscience. *Nature Neuroscience*, 17:1440–1441.
- 498 [34] Snyder, A. Z. (1991). Dipole source localization in the study of EP generators: a critique.
499 *Electroencephalography and Clinical Neurophysiology*, 80(4):321–325.
- 500 [35] Solomon, E. A., Gross, R., Lega, B., Sperling, M. R., Worrell, G., Sheth, S. A., Zaghloul,
501 K. A., Jobst, B. C., Stein, J. M., Das, S., Gorniak, R., Inman, C., Seger, S., Kragel, J. E., Rizzuto,

- 502 D. S., and Kahana, M. J. (2018). Mtl functional connectivity predicts stimulation-induced
503 theta power. *Nature Communications*, In press.
- 504 [36] Sporns, O. and Betzel, R. F. (2016). Modular brain networks. *Annual Review of Psychology*,
505 67:613–640.
- 506 [37] Talairach, J. and Tournoux, P. (1988). *Co-planar stereotaxic atlas of the human brain*. Verlag,
507 Stuttgart.
- 508 [38] Tavor, I., Jones, O. P., Mars, R. B., Smith, S. M., Behrens, T. E., and Jbabdi, S. (2016). Task-
509 free MRI predicts individual differences in brain activity during task performance. *Science*,
510 352(6282):216–220.
- 511 [39] Turk-Browne, N. B. (2013). Functional interactions as big data in the human brain. *Science*,
512 342:580–584.
- 513 [40] Weidemann, C. T., Kragel, J. E., Lega, B. C., Worrell, G. A., Sperling, M. R., Sharan, A. D.,
514 Jobst, B. C., Khadjevand, F., Davis, K. A., Wanda, P. A., Kadel, A., Rizzuto, D. S., and Kahana,
515 M. J. (2018). Neural activity reveals interactions between episodic and semantic memory
516 systems during retrieval. *Journal of Experimental Psychology: General*, In press.
- 517 [41] Yeo, B. T. T., Krienen, F. M., Sepulcre, J., Sabuncu, M. R., Lashkari, D., Hollinshead, M.,
518 Roffman, J. L., Smoller, J. W., Zollei, L., Polimieni, J. R., Fischl, B., Liu, H., and Buckner,
519 R. L. (2011). The organization of the human cerebral cortex estimated by intrinsic functional
520 connectivity. *Journal of Neurophysiology*, 106(3):1125–1165.